Computational design of Co- and Fe-based CO_2 to jetfuel catalysts

Catarina Regra da Silva
catarina.da.silva@tecnico.ulisboa.pt

Instituto Superior Técnico, Lisboa, Portugal

October 2022

Abstract

The Fischer-Tropsch Synthesis is used to form hydrocarbons with syngas mixture (CO and H_2), but a CO_2 and H_2 feed can be used as well. In this work, Co- and Fe-based catalysts are studied with DFT calculations and for Co-based catalysts, a microkinetic model is used to study the FT mechanism. Cobalt bulk structures were analysed, FCC and HCP. On the Co(111) surface, CO adsorption was most stable at the top site with a value of -135kJ/mol. Furthermore, CO_2 activation with OH* and with H* was investigated on Co(111). HCOO* hydrogenation and dissociation reactions of CO_2, HCOO and COOH were also considered. Activation barriers and reaction energies were calculated for these reactions and energy profiles were constructed. It was seen that the path of CO_2 hydrogenation with OH* to form COOH* and subsequent dissociation to CO* and OH*, is the least energy required. A dual-site microkinetic model was used for 2 scenarios (single-site and dual-site) and for 2 different feed types, i.e., H_2/CO and H_2/CO_2, for 1 and 20bar. Overall, methane was the product with the highest selectivity. The iron carbide bulk structures analysed were χ-Fe_5C_2, ϵ-Fe_3C, η-Fe_2C and θ-Fe_3C. Cohesive and formation energies were calculated and the iron carbide with the lowest energies is η-Fe_2C. Surfaces were analysed for all bulk structures, and the impact of the Fe/C ratio on surface stability was investigated via the carbon chemical potential. Adsorption energies were calculated on the χ-Fe_5C_2(510) surface where CO adsorption energy is -1.97eV on Fe 3-fold site.

Keywords: CO_2 Hydrogenation, Jet Fuel, Cobalt, Iron Carbides, DFT calculations, Microkinetic Modelling

1. Introduction

The main sources of CO_2 emissions from human sources are in the industry (chemical, metallurgical, and mineral transformation processes), land use, forestry and agriculture, and the burning of fossil fuels (oil, natural gas and coal). The burning of fossil fuels is mainly to produce electricity and heat, in industries (on-site burning in facilities for energy) and in transportation.[1] For the past 10 years, ground transportation has become less dependent on fossil fuels, since the rise of batteries and the electrification of railways. For aviation, this approach is unsuitable. So for this sector, there is a pressing need to produce sustainable jet fuel to reduce CO_2 emissions. The volatile price of crude oil is an additional incentive to different jet fuel sources.[2] CO_2 hydrogenation converts CO_2 and H_2 into hydrocarbons. Since the objective is to produce sustainable jet fuel, the hydrogen (H_2) must come from a sustainable source as well (green hydrogen). Water electrolysis is a solution, knowing the energy applied in the electrolysis is from renewable sources (e.g. solar, wind). A lot of researchers are focusing on the development of electrolytic hydrogen systems as this review presents [3]. The objective is to have a circular supply of jet fuel. Capture and purification of CO_2 to further react with green H_2 in the presence of a catalyst producing jet fuel. This sustainable jet fuel is distributed to commercial and military airlines suffering engine combustion, releasing CO_2 going back in the cycle.

2. Methodology

2.1. Convergence Tests

Convergence tests were performed in bulk structures and slabs. The convergence was observed in the total energy without entropy of the system. To achieve more accurate results, simulation parameters were tested in the first stage. Those parameters are cut-off energy, k-points and smearing width. For the cut-off energy, the tag ENCUT was varied, typically ranging from 200-600 eV. Higher values are better but are computationally more expensive. The convergence criterion was set to 2 meV/atom. This was also done for the number of k-points (file KPOINTS), and the smearing width

(tag SIGMA). For smearing width, lower values frequently produce superior numerical precision depending on the smearing scheme (ISMEAR) but may come at the price of a more challenging convergence of the self-consistent field. The ISMEAR was set at 2 for Methfessel-Paxton order 2.

2.2. Geometry Optimisation

Geometry optimisation was performed for gas phase molecules, bulk structures and slab structures. For gas phase molecules, by using a cubic unit cell with dimensions of 15Å by 15Å by 15Å, the interactions between repeating unit cells (i.e., neighbouring molecules) were limited to a minimum. A plane–wave basis set was used with a cut–off kinetic energy of 450 eV. The Brillouin zone for the calculation of gas phase molecules was represented by the gamma point. For these calculations, PBE and VdW-DF functionals were used. Geometries were optimised until a change in energy of less than 0.01 eV/Åoccurred between consecutive steps.

Cobalt structures were also optimised and the parameter optimisation is for FCC-C, FCC-O and HCP-O a plane–wave basis set with a cut-off energy of 450, 500 and 500 eV, respectively. The samplings of the Brillouin zone were generated from the Monkhorst–Pack scheme with k-points of 11×11×11, 15×15×15 and 15×15×15, respectively. The smearing width for each bulk structure respectively was 0.2, 0.2 and 0.25 eV. The surface Co(111) was optimised using a plane–wave basis set with a cut-off energy of 450, using 3×3×1 Monkhorst–Pack grid of k-points and a smearing width of 0.2 eV. The iron carbide bulk structures were optimised using three different functionals, PBE, VdW-DF and SCAN-rVV10, and a plane–wave basis set with a cut–off kinetic energy of 500 eV. The smearing width for χ-Fe_5C_2, ϵ-Fe_3C and η-Fe_2C structures was 0.05 eV. As for the bulk θ-Fe_3C the smearing width used was 0.2 eV. The grids used were Monkhorst–Pack for χ-Fe_5C_2 (6×6×4, k-points), η-Fe_2C (8×6×6, k-points) and θ-Fe_3C (6×4×4, k-points), but for ϵ-Fe_3C (6×6×6, k-points) a gamma centred mesh was used. Iron carbide slabs were optimised using a plane–wave basis set with a cut–off kinetic energy of 450 eV and a smearing width of 0.2 eV. The k-points used were Monkhorst–Pack grids.

2.3. Transition State

The NEB calculations were performed with 5 or 8 intermediate images, depending on the reactions and the difficulty to find the transition state. The calculations were performed with the VdW-DF functional, a cut-off energy of 450 eV, a smearing width of 0.2 eV, and the Brillouin zone was sampled with a (3×3×1) Monkhorst-Pack grid. When cNEB was used POTIM[1]=0.015 and IBRION[2]=1 were used. The low POTIM resulted in a slow convergence towards the TS, but it resulted in a higher success rate for finding the TS. When POTIM was increased to 0.5, the TS can be found faster, but calculations often exploded (i.e., abnormal increase in energies).[4]

After the cNEB method, the dimer method can be used to further refine the TS. For example, when the structure found in the NEB calculations is not yet a TS but very close to one the dimer method can be employed to find the exact TS. To start the dimer method calculation, several scripts from VTST[4] were used, to generate automatically initial files, such as a POSCAR file at the interpolated saddle point and a MODECAR file providing the starting direction that passes through the NEB supposed saddle point. For a dimer calculation, some tags should be changed, such as IBRION=3, POTIM=0.0, IOPT=2 and ICHAIN=2.[4]

2.4. Result Analysis methods

The adsorption energy of an adsorbate species, e.g CO, on a metal surface may be estimated using equation 1.[5][6][7]

$$E_{adsorption} = E_{system} - E_{slab} - E_{adsorbate} \quad (1)$$

Where E_{system} is the energy of the system slab+adsorbate, the E_{slab} is the energy of the slab and the $E_{adsorbate}$ is the energy of the adsorbate in the gas phase. All these electronic energies are obtained from the VASP calculation of the optimised structures. The energy of adsorption is represented with $E_{adsorption}$, and it was converted to kJ/mol because VASP is in eV.

The cohesive energy (E_{coh}) of an iron carbide bulk structure was calculated with equation 2.

$$E_{coh} = \frac{N_{Fe}E_{Fe}^{gas} + N_C E_C^{gas} - E_{bulk}}{N_{Fe} + N_C} \quad (2)$$

The E_{bulk} is the electronic energy of the bulk structure, and the N_{Fe} and N_C are the amount of Fe and C atoms, respectively. The E_{Fe}^{gas} is the electronic energy of a single Fe atom in the gas phase, and E_C^{gas} is the electronic energy of a single carbon atom in the gas phase.

The formation energy (E_{form}) was calculated from the equation 3, where the μ_C is the chemical potential of carbon. The E_{Fe}^{gs} is the electronic energy of a single Fe atom in the BCC bulk structure (ground state).

$$E_{form} = \frac{E_{bulk} - N_{Fe}E_{Fe}^{gs} - N_C\mu_C}{N_{Fe} + N_C} \quad (3)$$

[1] Ionic step size scaling.

[2] Defines the method for updating and moving the ions.

The surface energy for the iron carbide surfaces was calculated using one of the two following equations. When a surface is stoichiometric, equation 4 is used. When it is non-stoichiometric, equation 5 is used, which includes the chemical potential of carbon. Preferably symmetric surfaces are used to accurately represent the surface energy. When asymmetric surfaces are used this is mentioned.

$$E_{surf.}^{stoich.} = \frac{E_{slab}(Fe_xC_y) - nE_b(Fe_aC_b)}{2A} \quad (4)$$

$$E_{surf.}^{non-stoich.} = \frac{E_{slab}(Fe_xC_y)}{2A} - \frac{nE_b(Fe_aC_b) - (y - x/(a/b))\mu_C}{2A} \quad (5)$$

The surface energy calculated is $E_{surf.}$ (J/m^2), either $E_{surf.}^{stoich.}$ for stoichiometric surfaces or $E_{surf.}^{non-stoich.}$ for non-stoichiometric surfaces. The $E_{slab}(Fe_xC_y)$, refers to the total slab electronic energy of Fe_xC_y (in eV), where contains n times the number of bulk unit cells. The bulk electronic energy of Fe_aC_b is $E_b(Fe_aC_b)$, and a/b is the Fe/C ratio of the bulk structure. The area of the surface (A) has units m^2 and the μ_C is the carbon chemical potential (eV). The calculation for the non-stoichiometric surfaces accounts for the carbon contribution in the surface energy, including the difference between carbon atoms on the slab and on the bulk structure multiplying that difference with the carbon chemical potential.

The carbon chemical potential varies depending on the atmosphere and with that obtains different values. The C in the catalyst is handled at thermodynamic equilibrium with the mixture of reactant and product (e.g., CO, H_2, C_2H_4, and H_2O) under FTS conditions, from which the μ_C may be deduced. So μ_C can be defined in a range with a maximum value from the reactant-catalyst equilibrium in equation 6, and a minimum value from product-catalyst equilibrium in equation 7.[8] Where $E0_C$ is the electronic energy for a carbon atom in a large unit cell. For typical FT conditions, the temperature is 523 K and the partial pressure of the gas phase of CO, H_2, H_2O and C_2H_4 are 0.83 MPa, 1.67 MPa, 0.09 MPa and 0.3 MPa, respectively. The p_0 was 0.1 MPa. The respective chemical potential calculated with PBE for carbon atoms is -7.56 eV (μ_C^{min}) and -6.65 eV (μ_C^{max}). The DFT values from Liu et al.[8] with PBE were -7.45 to -6.60 eV also from the same equations.

$$\mu_C^{max} = \mu_{CO} + \mu_{H_2} - \mu_{H_2O} - E0_C \quad (6)$$

$$\mu_C^{min} = \frac{1}{2}\mu_{C_2H_4} - \mu_{H_2} - E0_C \quad (7)$$

2.5. Microkinetic Modelling

The microkinetic modelling software used was Chemkin®, which is software to solve complex problems of chemical kinetics. The simulations performed in Chemkin were with a plug-flow reactor and 2 different types of feed were tested. One is H_2/CO=2/1 and the other is H_2/CO_2=2/1. The catalyst used was cobalt pure metal with terrace and edge sites. The simulations were set to achieve a conversion of 10% of CO or CO_2, depending on the feed. The reactor temperature was set at 500 K. Two scenarios were tested with a dual-site catalyst or single-site catalyst, at 1 bar and 20 bar.

3. Results & discussion

3.1. Co-based catalyst

3.1.1 Bulk structures

The results for FCC-C from calculations in Table 1 differ from the experimental values ([10][9]) by 0.3%. Earlier reported DFT results for lattice constant is 3.538Å[11] for FCC-C which differs 0.012Å from the experimental value, while our value differs 0.011Å, from the experimental value (3.55Å). For the HCP-O structure, the difference between calculated and experimental values of the lattice constant a is 0.6%. The functional used in the calculations was VdW-DF and the functional used in [11] was PW91. The difference between the experimental lattice constant and our DFT calculated value can be explained by the fact that VdW-DF is less accurate in describing the Metal-Metal bond interactions. The bulk modulus calculated for the HCP structure differs significantly from the experimental value of 191 GPa by 7%.

3.1.2 Surface Co(111)

For investigating CO_2 activation, the Co(111) surface was selected with 3 layers. CO adsorption energy was calculated on 4 different active sites, top, bridge, fcc and hcp sites. The most stable structure is CO adsorbed on the top site, with a value of -135 kJ/mol (energy not corrected). From the corrected values the most stable adsorption site is the hcp site in a slab with 3 layers with a corrected value of -130 kJ/mol (and on top adsorption has a value of -129 kJ/mol). Nonetheless, when comparing (table 3) the sites with a larger slab (4 layers) the stable site is the top site with a corrected energy of -119 kJ/mol. The VdW-DF functional accurately predicts the correct adsorption site from the experiment.

Table 1: Optimised bulk structures with VdW-DF functional and equation of state results.

	a*(exp.)	b*	c*(exp.)	V (Å^3)*	V (Å^3)**	E (eV)**	B (GPa)**(exp.)
FCC-C	3.561 (3.55)[9]	3.561	3.561	45.17	45.77	-14.397	164.95
FCC-O	2.475	2.475	3.5	21.44	22.84	-7.195	164.58
HCP-O	2.524(2.51)[10]	2.524	4.072(4.07)[10]	44.95	45.09	-14.496	178.17(191)[10]

* Optimised values from VASP simulation.
** Optimised values from EOS estimation of Murnaghan.

Table 2: Activation energies from DFT (VdW-DF), Gibbs free energy barriers and Gibbs free energies of reaction for studied reactions and their transition states.

IS FS	CO_2*+* CO*+O*	CO_2*+OH* COOH*+O*	CO_2*+H* HCOO*+*	CO_2*+H* COOH*+*	HCOO*+H* HCOOH*+*	HCOO*+* O*+HCO*	COOH*+* CO*+OH*
TS	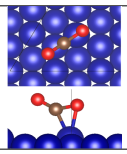	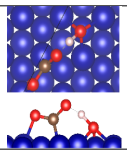	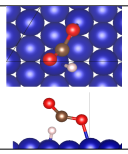	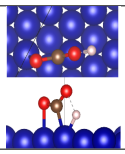	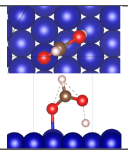	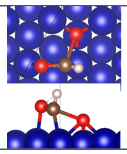	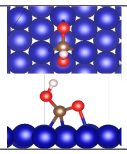
Activation Energy (kJ/mol)	70	55	102	154	108	92	22
ΔG activation (kJ/mol)	69	57	98	150	98	87	6
ΔG reaction (kJ/mol)	-80	45	6	62	63	35	-125

Table 3: Adsorption energies (E_{ads} values including ZPE in parentheses) of CO adsorption on top, fcc, hcp and bridge sites of Co(111).

	Calculated (with ZPE) (kJ/mol)	
CO adsorption	3 layers	4 layers
top	-135 (-129)	-126 (-119)
fcc	-131 (-127)	-116 (-113)
hcp	-134 (-130)	-120 (-116)
bridge	-127 (-123)	-120 (-116)*

* CO adsorbed molecule shifted positions from bridge site to hcp site.

The CO_2 hydrogenation over a catalyst can be predicted by testing several reaction pathways computationally. The transition states found were the CO_2 hydrogenation with OH and with H, HCOO hydrogenation and dissociation reactions of CO_2, HCOO and COOH.

The activation energy and the reaction energy were calculated at 0.1 MPa and 500 K. Table 2 summarises calculated activation energies from DFT electronic energies, Gibbs free energies of activation and reaction free energies.

In figure 1, the energy profile for the reactions studied is presented. The mixture CO_2+2*+OH*+H* is chosen as a reference state (IS, which is the 0 value). Energies for important intermediates and transition states are indicated. It is seen that the path of CO_2 hydrogenation with OH* to form COOH* followed by its dissociation to CO* and OH* is the least energy required.

3.1.3 Microkinetic Modelling

The microkinetic model used in Chemkin was the same as implemented by Gunasooriya [5] (dual-site microkinetic model), where reactions on cobalt terrace sites were at low coverage and the reactions on B_5 step sites (edge sites) are at high coverage, but results should not be affected. In future work, these reactions should also be calculated at low coverages. The microkinetic model was studied with either CO or CO_2 as feeds. With a pressure of 1 or 20 bar for cobalt catalyst pure metal at low coverage, 2 scenarios were analysed:

A. Single site catalyst - Only terrace sites present.

B. Dual site catalyst - Both terrace and edge (10%) sites present.

CO feed

The CO feed (H_2/CO=2/1) was analysed for low CO coverage for the 2 scenarios. The results are present in table 4. For all cases, the main product is methane, at 1 bar the methane selectivity is 87% for scenario **A**, and 99.9% for scenario **B**.

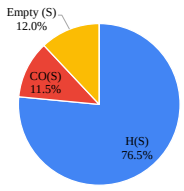

(a) Scenario **A - 1bar**

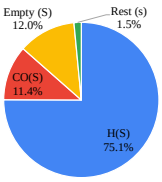

(b) Scenario **B - 1bar**

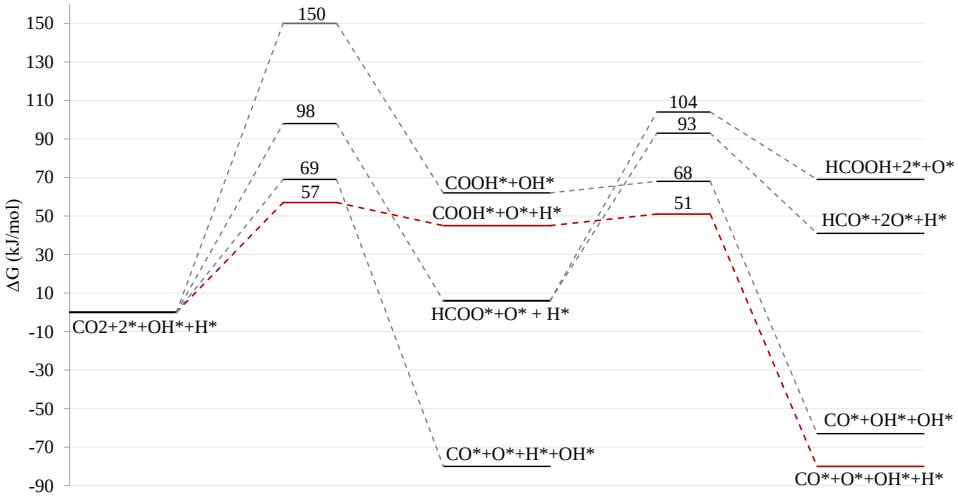

Figure 1: ΔG energy profile of the reactions studied which form a pathway for CO_2 hydrogenation on Co(111).

Table 4: Results from the low coverage model in Chemkin with a CO feed at the specified pressure.

Scenario	Pressure (bar)	CO conversion (%)	TOF (s^{-1})	CH_4	CO_2	C_1-C_4*
A	1	10.04	1.72E-05	86.75%	13.25%	0.00%
A	20	10.04	4.01E-05	91.51%	8.42%	0.08%
B	1	10.05	0.253	99.85%	0.15%	0.00%
B	20	10.04	2.30	99.96%	0.04%	0.00%

* C_1 molecules with the exception of CO_2 and CH_4.

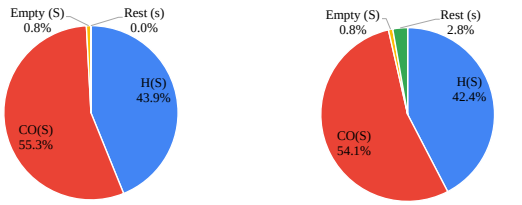

(c) Scenario **A - 20bar** (d) Scenario **B - 20bar**

Figure 2: CO feed results on surface coverages (S stands for terrace site) of CO, H, rest of the molecules and empty terrace site for scenario **A**, and scenario **B** at 1 bar and 20 bar.

The scenario **A** at 20 bar presents a 0.08% selectivity for C_1-C_4 molecules. Also, scenario **A** produces a higher CO_2 content than scenario **B**, the increase in pressure seems to reduce CO_2 formation and the addition of edge sites also decreases the CO_2 production.

At both 1 and 20 bar, scenario **B** presents a high TOF, of 0.253 and 2.30 s^{-1}, respectively. The addition of edge sites favours methane formation. At these conditions, this catalyst is suitable for methanation. The surface coverages are presented in figure 2, where the terrace site coverages are higher. As for the coverage of the edge site in scenario **B** is 99.9%(1 bar) and 95.5%(20 bar) empty. The terrace coverage of CO and H is quite the same for both scenarios, with the exception of a small percentage of terrace sites that are covered with other intermediates (up to C_3 alkanes, alkenes, alcohols, ketones and aldehydes). The increase in pressure to 20 bar makes the coverage of CO on the terrace site increase (approximately 44% increase), and the coverage of H on the terrace site (approximately 33% decrease) and empty terrace site both decrease. At high pressure, CO coverage is higher than the coverage used in DFT (1/9ML). So the high CO coverage on the terrace site with high pressure (20 bar) is an invalid calculation because DFT calculations would be needed at higher CO coverages. The H coverage obtained in the microkinetic model is higher than the H coverage in DFT calculations. DFT calculations of H at high coverage are needed to better assess the high coverage adsorption energy of H. The overestimated H coverage is partially responsible for high methane selectivity.

CO_2 feed

The CO_2 feed (H_2/CO_2=2/1) was also analysed for both scenarios. Table 5 presents the results obtained. As seen the main product formed is CO for the single-site scenario. When increasing the pressure to 20 bar the production of CH_4 increases and CO decreases. The addition of edge sites also increases the production of methane, as predicted with CO feed.

In none of the scenarios presented and pressure tested the C_1-C_4 selectivity goes past 0.00%. However, in scenario **A** at 1 bar the CO selectivity reaches 81.7%, which suggests a possible high CO formation on the catalyst. The coverages seen

Table 5: Results from the low coverage model in Chemkin with a CO_2 feed at the specified pressure.

Scenario	Pressure (bar)	CO conversion (%)	TOF (s^{-1})	CH_4	CO	C_1-C_4
A	1	10.00	1.36E-06	18.31%	81.69%	0.00%
A	20	10.11	1.81E-06	88.28%	11.72%	0.00%
B	1	9.97	1.35E-06	99.99%	0.01%	0.00%
B	20	10.04	1.73E-06	100.00%	0.00%	0.00%

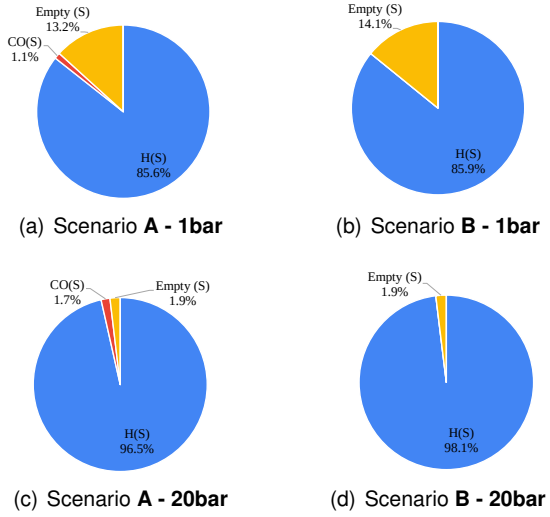

(a) Scenario **A - 1bar** (b) Scenario **B - 1bar**

(c) Scenario **A - 20bar** (d) Scenario **B - 20bar**

Figure 3: CO_2 feed results on surface coverages (terrace site) of CO, H, rest of the molecules and empty terrace site for scenario **A**, and scenario **B** at 1 bar and 20 bar.

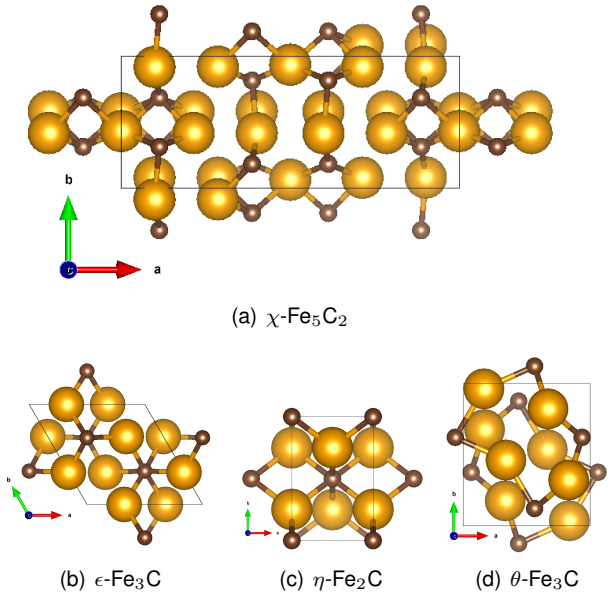

(a) χ-Fe_5C_2

(b) ϵ-Fe_3C (c) η-Fe_2C (d) θ-Fe_3C

Figure 4: Iron carbides bulk structures studied. The yellow and brown atoms represent the Fe and C atoms, respectively.

show that the increase in pressure increases H coverage on the terrace site. The addition of edge sites decreases CO coverage on the terrace sites. The edge site remains empty at 1 and 20 bar for scenario **B**.

For CO hydrogenation, the TOF is higher compared to the TOF obtained from CO_2 hydrogenation in all scenarios and pressures. But for scenario **B** the TOF is much higher in CO hydrogenation. For both CO and CO_2 hydrogenation, methane is the product with the higher selectivity. However, for CO_2 hydrogenation, in scenario **A** at low pressure the CO presents a high selectivity. The CO_2 hydrogenation presents a low CO coverage compared to CO hydrogenation. The H coverage for both reactions is high, but for CO_2 hydrogenation it is high in both scenarios and pressures. So DFT calculations of H at high coverage would be needed in order to build a more accurate microkinetic model.

3.2. Fe-based catalysts

3.2.1 Bulk structures

The results of the geometry optimisation for each bulk structure are in table 6, including DFT and experimental results from the literature.

As seen in table 6, the results are in agreement with DFT values and experimental values. The DFT values in ref. [12] are also obtained with the PBE functional. The calculated cohesive energies compared to Hyodo et al.[12] present a maximum absolute difference of 0.24 eV/atom (which is a 4% difference) in all bulk structures. In this work, the calculated values are higher in all cases, which can be due to different settings used in the simulations.

Formation energies of the analysed bulk structures are available in table 7 for different carbon chemical potentials, including literature (from Liu et al.[8]) values to compare. It is seen that the formation energy decreases with an increase in carbon chemical potential. The formation energy of $\eta - Fe_2C$ is the lowest which is also confirmed by Liu et al., which can be considered the most stable bulk structure compared to the others. The $\chi - Fe_5C_2$ is the next structure with low formation energy.

3.2.2 Surfaces

ϵ-Fe_3C

The ϵ-Fe_3C surfaces studied are $(001)_{0.0}$, $(011)_{0.0}$ and $(101)_{0.0}$. The most stable surface according to calculations is the $(101)_{0.0}$ with a surface energy of 2.32 J/m^2 (PBE), however, accord-

Table 6: Iron carbide bulk structures lattice constants, optimal volume, bulk modulus and cohesive energy from this work, DFT reference and experimental values.

		a (Å)	b (Å)	c (Å)	V (Å^3)	B (GPa)	E_{coh}(eV/atom)
	This work[1]	4.662	4.662	4.32	80.6	209.27	-5.69
ϵ-Fe_3C	DFT[12]	4.548	4.548	4.286		175	-5.48
	Exp.[13]	4.767	4.767	4.354	98.9		
	This work[1]	4.714	4.282	2.824	56.6	245.55	-5.93
η-Fe_2C	DFT[12]	4.496	4.262	2.766		197	-5.72
	Exp.[14]	4.704	4.318	2.830			
	This work[1]	11.593	4.493	4.976	258.0	240.37	-5.79
χ-Fe_5C_2	DFT[12]	10.679	4.493	4.957		219	-5.60
	Exp.[15]	11.562	4.573	5.0595	265.1		
	This work[1]	5.016	6.734	4.470	151.3	230.78	-5.69
θ-Fe_3C	DFT[12]	4.979	6.315	4.491		209	-5.45
	Exp.[16]	5.088	6.742	4.526	155.3	175	

Table 7: Formation energies for each iron carbide bulk structure with two different chemical potentials of carbon. PBE functional was used for calculations and also for Liu et al. values.[8]

	$\epsilon - Fe_3C$	$\eta - Fe_2C$	$\chi - Fe_5C_2$	$\theta - Fe_3C$
μ_C=-6.65 eV	-0.602	-0.816	-0.696	-0.605
μ_C=-7.56 eV	-0.375	-0.513	-0.436	-0.378
μ_C=-6.60[8] eV		-0.840	-0.81	-0.75

ing to Broos et al.[17] the most stable surface is the $(001)_{0.0}$ with a surface energy of 1.58 J/m^2 (PBE). Broos et al. made the surfaces according to the ϵ-Fe_2-0.25C bulk structure, which presents a higher carbon content. Thus, the surfaces from Broos et al. present a lower Fe/C ratio of 2 compared to a Fe/C ratio of 3 of the surfaces calculated in this work. The presence of higher carbon content on the surface increases surface stability.

Figure 6 shows the relation of the surface energy with the chemical potential. As seen, the $\epsilon(001)_{0.0}$ presents a high surface energy compared to $\epsilon(011)_{0.0}$ and $\epsilon(101)_{0.0}$ surfaces. Since these surfaces are non-stoichiometric, the surface $\epsilon(001)_{0.0}$ presents a ratio Fe/C=4.5, while the other two surfaces have a ratio Fe/C=3.25. This suggests that the higher carbon content on the surface stabilises the surface.

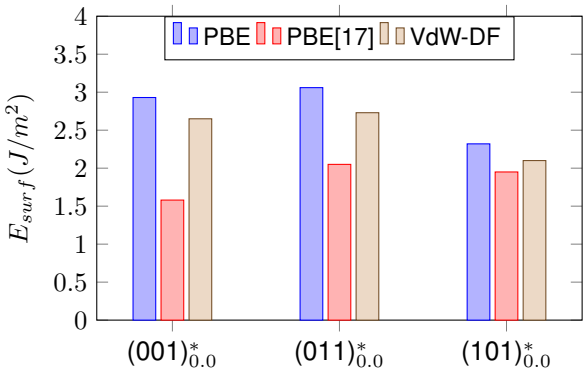

Figure 5: Surface energy of ϵ-Fe_3C asymmetric surfaces for PBE, VdW-DF and SCAN-rVV10 functionals and reference values. (*) Asymmetric and stoichiometric surfaces.[17]

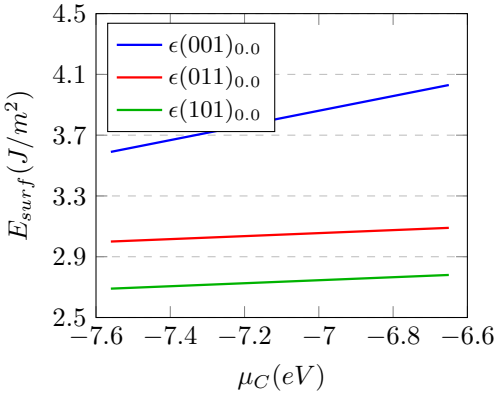

Figure 6: Surface energy of non-stoichiometric surfaces of ϵ-Fe_3C with varying chemical potential of carbon. Calculated with PBE functional.

χ-Fe_5C_2

The χ-Fe_5C_2 surfaces are $(100)_{0.0}$, $(100)_{0.287}$, $(010)_{0.25}$, $(11\bar{1})_{0.0}$, $(11\bar{1})_{0.5}$ and $(510)_{0.0}$. Figure 7 shows that the most stable surface calculated is the $(510)_{0.0}$ (2.07 J/m^2, PBE) according to all functionals and Liu et al.[8]. The value of surface energy from Liu et al. of $(510)_{0.0}$ is 1.75 J/m^2, and the Fe/C ratio is 2, while for the surface in this work the ratio is 2.5, which could explain why the value from this work is higher. The (510) surface from Liu et al. suffered a reconstruction, extra C atoms arrived to occupy the 4-fold Fe vacant sites. This reconstruction was discovered by the stochastic surface walking (SSW) neural network (NN) potential developed by the group of Liu et al., by iterative self-learning method of SSW-NN data set.

As expected the surface $(100)_{0.0}$ (Fe/C=3) is more stable than $(100)_{0.287}$ (Fe/C=3.5), since it presents a lower Fe/C ratio. The bulk structure presents a Fe/C ratio of 2.5, and the non-

stoichiometric surfaces studied present a higher Fe/C ratio, which explains the increase of surface energy with the increase of carbon chemical potential.

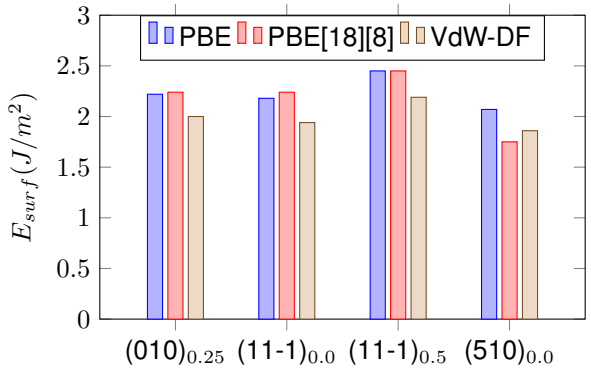

Figure 7: Surface energy of χ-Fe_5C_2 surfaces for PBE, VdW-DF and SCAN-rVV10 functionals and reference values. (*) Asymmetric and stoichiometric surfaces.[18][8]

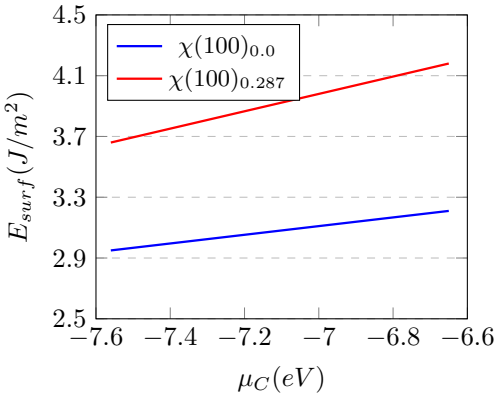

Figure 8: Surface energy of non-stoichiometric surfaces of χ-Fe_5C_2 with varying chemical potential of carbon. Calculated with PBE functional.

3.2.3 Adsorption of molecules on χ-Fe_5C_2(510)

Adsorption of CO, C, O, H, OH and H_2O was tested on $\chi(510)_{0.0}$ sites, using the PBE functional. A smearing width of 0.2 eV, a Monkhorst-Pack grid of 4×2×1 k-points and a plane wave cut-off energy of 450 eV were used for the simulations. The electronic energies of H (eq. 8), O (eq. 9), C (eq. 10) and OH (eq. 11) were calculated following the reactions below, using the electronic energies of the known molecules (H_2, H_2O, CO).

$$\frac{1}{2}H_2 \longrightarrow H \tag{8}$$

$$H_2O \longrightarrow H_2 + O \tag{9}$$

$$CO + H_2 \longrightarrow C + H_2O \tag{10}$$

$$H_2O \longrightarrow \frac{1}{2}H_2 + OH \tag{11}$$

Table 8: Calculated adsorption energies (E_{ads}, eV) of molecules on $\chi(510)_{0.0}$ surface with a coverage of 1/40 ML‡. Calculated with PBE functional.

Sites	CO	H*	O*	C*	OH*
C4f	-1.73†	-2.30†	0.40	-0.94	-0.39†
F3f	-1.73†	-2.31	0.38	-1.24	-0.19†
CFb	-	-1.96†	-	-0.69	-
Fb	-1.97†	-2.31†	-0.10†	-1.46†	-0.19
Ct	-0.98	-1.96	0.49†	-0.76†	0.46
Ft	-	-	-	-1.46†	-

* Electronic energy calculated through the respective formation reaction.
† Shifts from the original position.
‡ The coverage is the number of adsorbed species over the number of exposed layer iron atoms.[19]

Table 8 shows the adsorption energies of some molecules on different sites. Most of the adsorbed structures shifted to more stable geometries. The CO is most stable and adsorbed in a Fe 3-fold site with an adsorption energy of -1.97 eV. Pham et al.[20], reports an adsorption value for the same site (3F-3) of -1.99 eV.

Due to the calculated energies being very negative, the coverage of CO and C on this surface ($\chi(510)_{0.0}$) under FTS conditions will be high. Consistent with the high surface energy (2.07 J/m^2, PBE).

4. Conclusions

The DFT analysis of Co- and Fe-based catalysts was the main objective of this work. For the Co-based catalyst, several reaction pathways involved in the FT process were analysed. Further, microkinetic modelling of a Co-based catalyst in a PFR reactor with CO or CO_2 feed was performed. For Fe-based catalysts, several iron carbides were studied with DFT calculations.

First, the Co-based catalyst was studied. The bulk structures analysed were FCC-C, FCC-O and HCP-O. The VdW-DF functional used to perform geometry optimisation seemed to be reliable when compared to experimental values. The adsorption of CO on the top site of a Co(111) surface with 3 layers is more stable compared to the other sites. However, stability on the top site is more reliable on Co(111) slabs with more than 3 layers.

Transition states were found when performing NEB calculations on Co(111) with 3 layers. From these transition states, energy barriers and reaction energies were calculated, and an energy profile was constructed. The reaction of CO_2 hydrogenation with OH* to COOH* followed by its dissociation to CO* and OH*is the most favourable. Direct CO_2 dissociation is the most favoured among the other competing reactions. The lower the energy of the pathway to produce CO* and CH* the better, since these are monomers in FTS.

The microkinetic model for both the CO feed and CO_2 feed, and at 1 and 20 bar, proved to be favourable for methane production. However, the

model was not valid anymore for higher pressures in the case of CO feed because of the high CO coverage, so a model including DFT calculations at higher CO coverage is necessary. DFT calculations of H at high coverage are needed as well to better assess the high coverage adsorption energy of H.

The Fe-based catalysts analysed were from the bulk structures χ-Fe_5C_2, ϵ-Fe_3C, η-Fe_2C and θ-Fe_3C. The analysis showed that the bulk structure with the lowest cohesive and formation energies is η-Fe_2C followed by χ-Fe_5C_2. Surfaces were analysed for each bulk structure and surface energies were calculated. The general conclusion from the surface energies analysed is that the Fe/C ratio plays an important role in surface stability, which is related to the carbon content on the surface. The surface with a high carbon content makes the surface energy decrease with an increase of the carbon chemical potential, and the opposite happens for the surfaces with low carbon content. So, carbon chemical potential also affects the surface energy, but this method of calculation, with μ_C, was only used for non-stoichiometric surfaces. When the surface has less carbon content than its bulk structure, the surface energy increases when the chemical potential increases. If the surface has more carbon content than its bulk structure, the increase in chemical potential will decrease the surface energy.

The surface $(510)_{0.0}$ is the most stable surface of the $\chi - Fe_5C_2$ surfaces studied. And on this surface, the CO adsorption energy is -1.97 eV on Fe 3-fold site, called the 3F-3 site by Pham et al.[20] where the adsorption is -1.99 eV. The adsorption energy achieved has a relative difference of 1.2% compared to the value of Pham et al. From the calculated energies of other molecules (H* and C* adsorption) because they are very negative, the coverage of CO and C on this surface ($\chi(510)_{0.0}$) under FTS conditions will be high. This is to be expected from the high surface energy of this surface (2.07 J/m^2, PBE).

References

[1] Global greenhouse gas emissions data. US EPA - United States Environmental Protection Agency, 2022. https://www.epa.gov/ghgemissions/global-greenhouse-gas-emissions-data.

[2] Pires et al. Alternative jet fuel properties. *BioResources*, 13(2):2632–2657, 2018.

[3] Mohd Fadhzir Ahmad Kamaroddin, Nordin Sabli, Tuan Amran Tuan Abdullah, Shamsul Izhar Siajam, et al. Membrane-based electrolysis for hydrogen production: A review. *Membranes*, 11(11), 2021. https://www.mdpi.com/2077-0375/11/11/810.

[4] Transition state tools for VASP-VTST. Theory.cm.utexas.edu. https://theory.cm.utexas.edu/vtsttools/index.html.

[5] Kasun Thanthrige. *Theoretical Study of the Mechanism and Microkinetics of Cobalt-Catalyzed Fischer-Tropsch Synthesis*. PhD thesis, Universiteit Gent, Laboratorium voor Chemische Techniek, Technologiepark 914, B-9052 Gent, België, 2018.

[6] Lakshmikanth K. G, Ishak Kundappaden, and Raghu Chatanathodi. A DFT study of CO adsorption on pt (111) using van der waals functionals. *Surface Science*, 681:143–148, 2019. https://doi.org/10.1016/j.susc.2018.12.001.

[7] W. Gao, Y. Chen, B. Li, et al. Determining the adsorption energies of small molecules with the intrinsic properties of adsorbates and substrates. *Nat Commun*, 11(1196), 2020. https://doi.org/10.1038/s41467-020-14969-8.

[8] Qian-Yu Liu, Cheng Shang, and Zhi-Pan Liu. In situ active site for CO activation in Fe-catalyzed fischer–tropsch synthesis from machine learning. *Journal of the American Chemical Society*, 143(29):11109–11120, 2021. DOI: 10.1021/jacs.1c04624.

[9] Neil W Ashcroft and N David Mermin. *Solid state physics*. Saunders College, 1976.

[10] Michael J. Mehl and Dimitrios A. Papaconstantopoulos. Applications of a tight-binding total-energy method for transition and noble metals: Elastic constants, vacancies, and surfaces of monatomic metals. *Physical Review B*, 54(7):4519–4530, 1996. DOI: 10.1103/physrevb.54.4519.

[11] Pieter van Helden, Ionel M. Ciobîcă, and Roelof L.J. Coetzer. The size-dependent site composition of FCC cobalt nanocrystals. *Catalysis Today*, 261:48–59, 2016. https://doi.org/10.1016/j.cattod.2015.07.052.

[12] Katsutoshi Hyodo, Shinji Munetoh, and Toshihiro Tsuchiyama. Empirical interatomic potential for Fe-C system using original Finnis-Sinclair potential function. *Computational Materials Science*, 184:109871, 2020. https://doi.org/10.1016/j.commatsci.2020.109871.

[13] Sigemaro Nagakura. Study of metallic carbides by electron diffraction part III. iron carbides. *Journal of the Physical Society of Japan*, 14(2):186 – 195, 1959. DOI: 10.1143/JPSJ.14.186.

[14] Y. Hirotsu and S. Nagakura. Crystal structure and morphology of the carbide precipitated from martensitic high carbon steel during the first stage of tempering. *Acta Metallurgica*, 20(4):645–655, 1972. https://doi.org/10.1016/0001-6160(72)90020-X.

[15] K. JACK and S. WILD. Nature of χ-carbide and its possible occurrence in steels. *Nature*, 212:248–250, 1966. https://doi.org/10.1038/212248b0.

[16] H.P. Scott, Q. Williams, and E. Knittle. Stability and equation of state of Fe_3C to 73 GPa: Implications of carbon in the earth's core. *Geophysical Research Letters*, 28(9):1875 – 1878, 2001. DOI: 10.1029/2000GL012606.

[17] Robin Johannes Petrus Broos. *Computational modelling of the Fischer-Tropsch reaction on iron carbides*. PhD thesis, Chemical Engineering and Chemistry, February 2020. Proefschrift.

[18] Robin J. P. Broos, Bart Zijlstra, Ivo A. W. Filot, and Emiel J. M. Hensen. Quantum-chemical DFT study of direct and H- and C-assisted CO dissociation on the χ-Fe_5C_2 Hägg Carbide. *The Journal of Physical Chemistry C*, 122(18):9929–9938, 2018. DOI: 10.1021/acs.jpcc.8b01064.

[19] Shu Zhao, Xing-Wu Liu, Chun-Fang Huo, Yong-Wang Li, Jianguo Wang, and Haijun Jiao. Determining surface structure and stability of ϵ-Fe_2C, χ-Fe_5C_2, θ-Fe_3C and Fe_4C phases under carburization environment from combined DFT and atomistic thermodynamic studies. *Catalysis, Structure & Reactivity*, 1(1):44–60, 2015. DOI: 10.1179/2055075814Y.0000000007.

[20] Thanh Hai Pham, Xuezhi Duan, Gang Qian, Xinggui Zhou, and De Chen. CO activation pathways of Fischer–Tropsch synthesis on χ-Fe_5C_2 (510): Direct versus hydrogen-assisted CO dissociation. *The Journal of Physical Chemistry C*, 118(19):10170–10176, 2014. DOI: 10.1021/jp502225r.